

Measurement of intrinsic and scattering attenuation of shear waves in two sedimentary basins and comparison to crystalline sites in Germany

Tom Eulenfeld and Ulrich Wegler

BGR Federal Institute for Geosciences and Natural Resources, Stilleweg 2, D-30655 Hannover, Germany. E-mail: tom.eulenfeld@bgr.de

Accepted 2016 January 20. Received 2016 January 20; in original form 2015 July 27

SUMMARY

We developed an improved method for the separation of intrinsic and scattering attenuation of seismic shear waves by envelope inversion called *Qopen*. The method optimizes the fit between Green's functions for the acoustic, isotropic radiative transfer theory and observed energy densities of earthquakes. The inversion allows the determination of scattering and intrinsic attenuation, site corrections and spectral source energies for the investigated frequency bands. Source displacement spectrum and the seismic moment of the analysed events can be estimated from the obtained spectral source energies. We report intrinsic and scattering attenuation coefficients of shear waves near three geothermal reservoirs in Germany for frequencies between 1 and 70 Hz. The geothermal reservoirs are located in Insheim, Landau (both Upper Rhine Graben) and Unterhaching (Molasse basin). We compare these three sedimentary sites to two sites located in crystalline rock with respect to scattering and intrinsic attenuation. The inverse quality factor for intrinsic attenuation is constant in sediments for frequencies smaller than 10 Hz and decreasing for higher frequencies. For crystalline rock, it is on a lower level and strictly monotonic decreasing with frequency. Intrinsic attenuation dominates scattering except for the Upper Rhine Graben, where scattering is dominant for frequencies below 10 Hz. Observed source displacement spectra show a high-frequency fall-off greater than or equal to 3.

Key words: Hydrothermal systems; Earthquake source observations; Seismic attenuation; Site effects; Wave scattering and diffraction.

1 INTRODUCTION

The MAGS2 project (microseismic activity of geothermal systems) aims at the observation, understanding and hazard analysis of induced earthquake activity at deep geothermal systems. In the scope of the project geothermal reservoirs in the sedimentary basins of the Upper Rhine Graben and the Molasse basin are monitored for induced seismic activity. The three geothermal plants in Landau, Insheim (Upper Rhine Graben) and Unterhaching (Molasse basin) already induced earthquakes with magnitudes up to M2.7. One major goal of the project is the calculation of shake maps and its uncertainties for induced earthquakes, leading to the problem of interpolation of peak ground velocity (PGV) measurements. Therefore, it is important to understand high-frequency wave propagation and attenuation properties of the medium between the hypocentres of induced events and the surface. Furthermore, as the three geothermal sites are located in sedimentary basins and the induced earthquakes rupture near the interface between sediments and bedrock, the presented study allows for insights into scattering and absorption properties of shear waves in sediments.

Attenuation of seismic waves, besides geometrical spreading, can be classified by the acting mechanism into intrinsic and scattering attenuation. Intrinsic attenuation is due to the absorption of seismic waves. Scattering attenuation is due to the redistribution of energy into different directions. Scattering is the reason why the seismic coda can be observed after the direct wave. Hoshiba *et al.* (1991) and Fehler *et al.* (1992) developed the multiple lapse time window analysis (MLTWA) which can be used to separate intrinsic and scattering attenuation. MLTWA calculates observed energy ratios between different time windows at various source–receiver distances. By a comparison to analytical results, the target parameters can be determined. Sens-Schönfelder & Wegler (2006) proposed an inversion of the complete *S*-wave envelope. Coda normalization is circumvented in the latter method as site effects and spectral source energy are determined by the inversion process. Both methods use solutions of radiative transfer theory to calculate scattering Green's functions and model seismogram envelopes. We use the inversion scheme for scattering and intrinsic attenuation of Sens-Schönfelder & Wegler (2006) and introduce several improvements to their method.

In this study, we focus on measurements of S -wave attenuation, because the S wave usually produces higher PGVs and is therefore more important for hazard analysis than the P wave. The structure of this publication is the following: Section 2 provides the procedures to calculate the observed and modeled energy density (i.e. envelope). Section 3 describes the inversion of earthquake observations for intrinsic and scattering attenuation. In Section 4, we introduce the MAGS2 data set, specify the parameters used in the inversion and present the obtained results. Results are discussed in Section 5. Finally, conclusions are drawn in Section 6.

2 MODELED AND OBSERVED ENERGY DENSITIES

Separating intrinsic and scattering attenuation is accomplished by making use of the different impact of each mechanism on the shape of the envelope. While homogeneous intrinsic attenuation is accountable for an exponential decrease in the envelope of the recordings, the most notable signature of scattering strength is the energy ratio of the direct arrival and the coda. We restrict ourselves to isotropic sources with the source function $W\delta(\mathbf{r})\delta(t)$, where W is the spectral source energy and δ the Dirac delta function. The energy density in a specific frequency band caused by this source can be calculated (Sens-Schönfelder & Wegler 2006, eq. 4) with

$$E_{\text{mod}}(t, \mathbf{r}) = WR(\mathbf{r})G(t, \mathbf{r}, \mathbf{g})e^{-bt}. \quad (1)$$

$R(\mathbf{r})$ is the energy site amplification factor (square of the amplitude site amplification factor). e^{-bt} describes the exponential intrinsic damping with time and depends on the intrinsic absorption parameter b . The Green's function $G(t, \mathbf{r}, \mathbf{g})$ accounts for the direct wave and the scattered wave field. \mathbf{g} is the vector of scattering parameters, whose length depends on the chosen representation of the Green's function. Dimensions for E_{mod} , W , R and G are $\text{Jm}^{-3}\text{Hz}^{-1}$, JHz^{-1} , 1 and m^{-3} , respectively.

Gaebler *et al.* (2015) compared different methods to calculate the Green's function using anisotropic elastic versus isotropic acoustic radiative transfer theory. For their data set results of the two methods for the transport mean-free path are the same within the inherent precision of the methods. Furthermore, they depict the impossibility to resolve different parameters of the scattering medium (namely, fluctuation strength and correlation length of the random media) for the elastic simulations because of their trade-off. In principle, our algorithm which will be described in Section 3 can be used to invert for a vector of multiple scattering parameters and is capable of using Green's functions determined by acoustic or elastic radiative transfer theory. Assured by the described findings of Gaebler *et al.* (2015), we choose the computationally cheap solution to calculate the Green's function for acoustic isotropic scattering in a homogeneous half-space. For simplicity, we use the analytic approximation of the solution for 3-D isotropic radiative transfer (Paasschens 1997). The Green's function then reads

$$G(t, r, g_0) = \exp(-v_0 t g_0) \left[\frac{\delta(r - v_0 t)}{4\pi r^2} + \left(\frac{4\pi v_0}{3g_0} \right)^{-\frac{3}{2}} t^{-\frac{3}{2}} \right. \\ \left. \times \left(1 - \frac{r^2}{v_0^2 t^2} \right)^{\frac{1}{8}} K \left(v_0 t g_0 \left(1 - \frac{r^2}{v_0^2 t^2} \right)^{\frac{3}{4}} \right) H(v_0 t - r) \right] \\ \text{with } K(x) = e^x \sqrt{1 + \frac{2.026}{x}}. \quad (2)$$

g_0 , the scattering coefficient, is the only scattering parameter used in this formula. Furthermore, v_0 is the mean S -wave velocity. The term with the Dirac delta function δ describes the direct wave, while the other term describes scattered waves. The relative error to the exact solution of acoustic isotropic radiative transfer provided by Zeng *et al.* (1991) is below 3 per cent (Ugalde & Carcolé 2009). The assumption of isotropic scattering is not valid for real media, anyway it is beneficial as the scattering coefficient g_0 determined with this wrong assumption can be interpreted as the transport scattering coefficient g^* in a more realistic anisotropic scattering scenario: $g^* = g_0$ (Gaebler *et al.* 2015).

The modeled envelope E_{mod} will be compared to observed envelopes at seismic stations. To obtain observed spectral energy densities, the velocity seismograms are filtered in a specific frequency band and later the envelope has to be normalized by the filter width Δf . The mean square velocity $\langle \dot{u}^2 \rangle$ is calculated from the filtered seismogram components \dot{u}_c with the help of the Hilbert transform H (Sato *et al.* 2012, p. 41)

$$\langle \dot{u}(t, \mathbf{r})^2 \rangle = \frac{1}{2} \sum_{c=1}^3 (\dot{u}_c(t, \mathbf{r})^2 + H(\dot{u}_c(t, \mathbf{r}))^2). \quad (3)$$

The observed energy density consisting of kinetic and potential energy is calculated by

$$E_{\text{obs}}(t, \mathbf{r}) = \frac{\rho_0 \langle \dot{u}(t, \mathbf{r})^2 \rangle}{C \Delta f} \quad (4)$$

with the mean mass density ρ_0 . Eq. (4) with $C = 1$ is valid for the full space. Because most stations are deployed on the surface, a free surface correction is introduced with a factor $C = 4$ (Emoto *et al.* 2010). Δf can usually be approximated by the difference between upper and lower corner frequency depending on the filter design. Here, we calculate Δf as the integral over the squared frequency response of the filter (Wegler *et al.* 2006). It has to be guaranteed that the coda of the earlier arriving P wave adds no significant contribution to the envelope of direct S wave and S coda. This is the case for our data set in the used frequency bands.

3 INVERSION FOR ATTENUATION PARAMETERS, SITE EFFECTS AND SOURCE PROPERTIES

Considering N_S stations (index i), N_E events (index j) and the observed energy densities for each event at each station with N_{ij} time samples (index k) in a specific frequency band, we want to minimize the error function

$$\epsilon(\mathbf{g}) = \sum_{i,j,k}^{N_S, N_E, N_{ij}} (\ln E_{\text{obs}ijk} - \ln E_{\text{mod}ijk}(\mathbf{g}))^2 \quad (5)$$

by optimizing \mathbf{g} . In each optimization step the equation system

$$\ln E_{\text{obs}ijk} = \ln E_{\text{mod}ijk}(\mathbf{g}), \quad (6)$$

or with eq. (1)

$$\ln E_{\text{obs}ijk} = \ln G(t_{ijk}, \mathbf{r}_{ij}, \mathbf{g}) + \ln R_i + \ln W_j - bt_{ijk}, \quad (7)$$

is solved for b , R_i and W_j . The equation system consists of $\sum_{i,j} N_{ij}$ equations and $N_S + N_E + 1$ variables. It is therefore overdetermined and solved by a least-squares approach. $\epsilon(\mathbf{g})$ is then given by the sum over the squared residuals of the solution. A problem arises from the multicollinearity between $\ln R_i$ and $\ln W_j$: multiplying W_j by an arbitrary factor and dividing R_i by the same factor leads to

the same equation system. Therefore, the relative level between W_j and R_i cannot be determined. This problem is dealt with by the substitutions

$$W_j = \tilde{W}_j W_1 \quad R_i = \tilde{R}_i / W_1. \quad (8)$$

\tilde{W}_1 equals 1 by definition and the resulting equation system in b , \tilde{R}_i and \tilde{W}_j ($j > 1$) can be solved without ambiguity. An additional constrained is needed to calculate W_1 . Here, we choose to fix the geometric mean GM of the station site corrections to 1. W_1 is then given by

$$W_1 = \frac{GM(\tilde{R}_i)}{GM(R_i)} = GM(\tilde{R}_i). \quad (9)$$

The other spectral source densities and site amplification factors can be obtained by eq. (8). Other constraints are possible, for example, the site amplification factor of a specific station could be fixed.

In the following, we want to specify which parts of the envelope are used for the samples t_{ijk} . It is important to include the direct wave in the inversion, because scattering strength mainly manifests in the energy ratio of direct wave and coda. Sens-Schönfelder & Wegler (2006) discuss that in weakly scattering media it is impossible to separate the two attenuation mechanisms only with information from the coda. While the separation of mechanisms is technically possible for strongly scattering media, inversion of real world imperfect data benefits from the inclusion of the energy arriving at and immediately after the S onset. Two time windows, a window including the direct S wave and a coda window are defined. Because of peak broadening and other effects (e.g. finite bandwidth), the onset of the observed envelope is delayed and generally has a completely different shape than the δ peak of the modeled envelope using isotropic radiative transfer. We solve this problem by comparing the mean observed and modeled energy density in the S -wave window. Sens-Schönfelder & Wegler (2006) discard models, in which these two values do not match. In contrast, in this study the direct wave is directly included in the least-squares inversion with a weight corresponding to the number of samples in the S -wave window. Of course, other weights are imaginable, for example, twice the weight of the S -wave window or the same weight as the coda window itself. We tried different possibilities, but did not find any substantial difference in the obtained results. Therefore, the most natural solution is used which fixes the weight to the number of samples in the S -wave window. In consequence, the sample t_{ij1} corresponds to the S -wave window and the other $N_{ij} - 1$ samples correspond to the coda window. The value of t_{ij1} is determined as a ‘balance point’ of the observed energy density in the S -wave window.

Other authors only use one time window with stronger smoothing containing coda and onset in a similar method (Padhy *et al.* 2007; Fielitz & Wegler 2015). This makes the method less complex, because the discrimination between direct S -wave window and coda window is omitted. However, it adds complexity at other places. It is unresolved how to deal with the fact that most energy in the theoretical Green’s function of isotropic radiative transfer is concentrated at the S onset in the form of the δ peak (assuming weakly scattering media) while the observed energy densities peak a considerable time after the S onset. This might cause a systematic error. We emphasize that this problem only arises because of the imperfections of the chosen Green’s function of isotropic radiative transfer. A Green’s function based on anisotropic scattering theory is expected to better fit the observations near the S onset. The approach of Padhy *et al.* (2007) and Fielitz & Wegler (2015) would be adequate for this kind of Green’s function. The simple and effective solution to the

mismatch of observed and isotropically modeled envelopes is to just use the averages in the S -wave time window as suggested by Sens-Schönfelder & Wegler (2006). Further advantages of this approach are the possibility to smooth the coda over a shorter time window and the possibility to adjust weights between coda and onset parts of the envelope. A comparison of both approaches for our data set shows only minor differences in the result.

Concluding, the inversion can be performed in the following manner:

(i) For fixed scattering parameters \mathbf{g} the Green’s functions $G_{ijk}(\mathbf{g})$ are calculated [e.g. with eq. (2) for the isotropic acoustic case] and the weighted least-squares system in eq. (7) is solved for b , \tilde{R}_i and \tilde{W}_j .

(ii) R_i , W_j and the sum of squared residuals $\epsilon(\mathbf{g})$ are calculated with eqs (9), (8) and (5).

(iii) Steps (i) and (ii) are repeated for different \mathbf{g} to find the optimal parameters \mathbf{g} , b , R_i and W_j by minimizing the error function ϵ . This step can involve a dedicated optimization algorithm to minimize computation time.

Fig. 1 illustrates the optimization procedure on the basis of a data example from the MAGS2 project for the isotropic acoustic case. The optimization is applied for different frequency bands with central frequencies f to determine the inversion results as a function of frequency.

We are interested in a statistical treatment of attenuation parameters. Therefore, each event will be inverted separately in Section 4 ($N_E = 1$). Because the geometric mean of site responses is fixed to one for every event, station site corrections R and spectral source densities W are not comparable for different events if a different set of stations is used for the inversion (e.g. due to the rejection of inapt data). This fact has to be corrected for. Each event is therefore scaled by a factor $1/c_j$ (j is event index) and the measured site amplifications for this event are scaled by c_j . Optimal c_j are obtained by solving a least-squares linear equation system which is constructed by the assumption that site amplification factors for one station and frequency are similar for different events. Assuming the site response at station i for event k is measured with R_{ik} , but for event l it has got a value of R_{il} , then the above condition translates to $R_{ik}c_k = R_{il}c_l$ or

$$\ln c_k - \ln c_l = \ln R_{il} - \ln R_{ik}. \quad (10)$$

Using event pairs $(k, k+1)$ and stations i eq. (10) represents a linear equation system for $\ln c_j$ for each frequency band. The geometric mean of site responses is again fixed at 1 to resolve ambiguity, but this time measurements of all events are involved.

The source displacement spectrum, seismic moment and moment magnitude can be calculated from the spectral source energy W as a function of frequency. The S -wave source displacement spectrum of a double-couple in the far-field is given by Sato *et al.* (2012, p. 188) as

$$\omega M(f) = \sqrt{\frac{5\rho_0 v_0^5 W}{2\pi f^2}}. \quad (11)$$

Seismic moment M_0 and corner frequency f_c can be obtained by fitting the observed source displacement spectrum to an assumed source model (Abercrombie 1995)

$$\omega M(f) = M_0 \left(1 + \left(\frac{f}{f_c} \right)^{\gamma n} \right)^{-\frac{1}{\gamma}}. \quad (12)$$

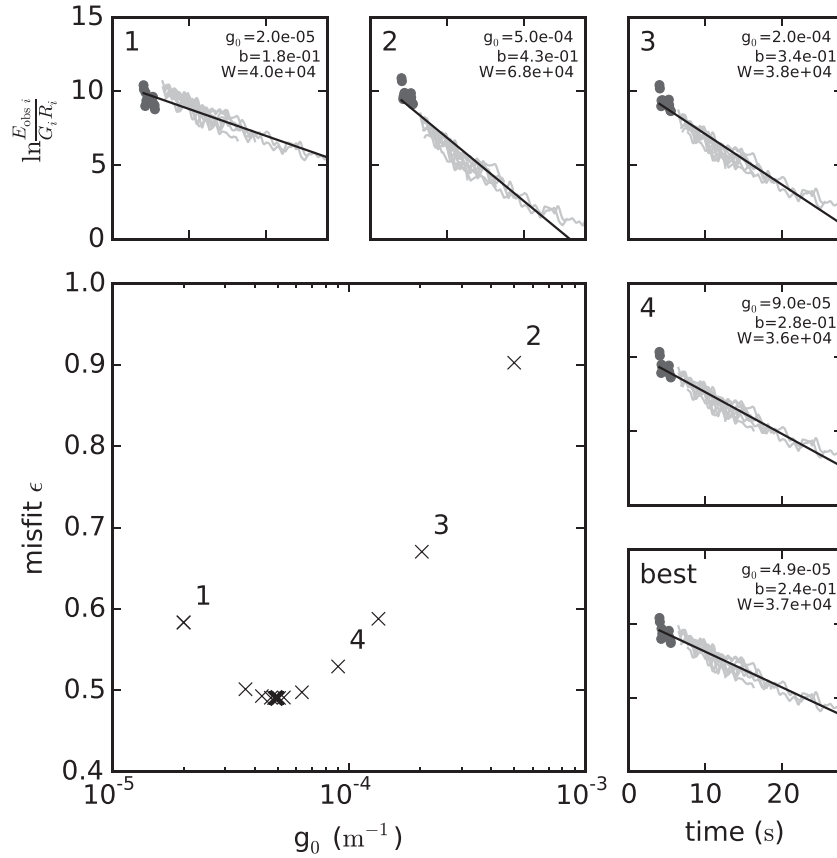


Figure 1. Illustration of the optimization procedure for a MAGS2 data set consisting of data from 11 stations and one event (2012 December 16, M1.4) in the frequency band 8–16 Hz. On the lower left-hand panel, the error function ϵ as a function of g_0 is displayed. The optimization was done by a Golden section search. Isotropic acoustic radiative transfer (eq. 2) is used to calculate the Green's function. The optimal value of $g = g_0$ is plotted with a thick cross. In the remaining panels, the least-squares solution of the weighted linear equation system (eq. 7) is displayed for the first four guesses and the optimal value of g_0 . Grey curves and dots represent the observed envelopes E_{obs} of coda and direct wave at the different sensors divided by the Green's function G . The envelopes are corrected for the obtained site corrections R_i . The straight line has a slope of $-b$ and an intercept of W and represents part of the right-hand side of the equation system. The lower right-hand panel for the best value of g_0 illustrates the low misfit of the equation system, that is, between the straight line and the vertically shifted envelopes.

n is the high-frequency fall-off and the shape parameter γ describes the sharpness of the transition between the constant level M_0 for low frequencies and the fall-off with f^{-n} for high frequencies. For $n = 2$, eq. (12) represents the source displacement spectrum of an omega square model. Taking the logarithm, eq. (12) transforms to

$$\ln \omega M(f) = \ln M_0 - \frac{1}{\gamma} \ln \left(1 + \left(\frac{f}{f_c} \right)^{\gamma n} \right). \quad (13)$$

An observed source displacement spectrum $\omega M(f)$ can be inverted for the four source parameters M_0 , f_c , n and γ by an optimization for f_c and γn and a simultaneous least-squares inversion of eq. (13) for $\ln M_0$ and $1/\gamma$. The sum of the squared residuals of the least-squares inversion are used as the cost function for the optimization in this case. The contribution of the energy of emitted P waves to the seismic moment is ignored. We justify this approach because the theoretical ratio of emitted S to P energy is larger than 20 for a double-couple source (Sato *et al.* 2012, p. 188). The relation between seismic moment M_0 in $\text{N} \cdot \text{m}$ and moment magnitude M_w is given by Hanks & Kanamori (1979)

$$M_w = \frac{2}{3} \log_{10} M_0 - 6.07. \quad (14)$$

Furthermore, transport scattering coefficient g^* and absorption parameter b can be converted to quality factors of scattering attenuation Q_{sc} and intrinsic attenuation Q_i with

$$Q_{\text{sc}}^{-1} = \frac{g^* v_0}{2\pi f} \quad Q_i^{-1} = \frac{b}{2\pi f}. \quad (15)$$

As previously mentioned, our inversion procedure is based upon the one presented by Sens-Schönfelder & Wegler (2006). Advantages over their approach are:

- (i) Instead of fitting a linear curve through $\ln E_{\text{obs}} - \ln G$ and calculating $W_j R_i$ afterwards, we simultaneously invert for b , R_i , W_j by solving the least-squares linear equation system.
- (ii) The direct wave is included with an appropriate weight instead of neglecting inapt models afterwards.
- (iii) We generalized the method to more than one event. Therefore, it is possible to use a single station with different events to estimate attenuation parameters.

We call this revised method *Qopen* (Separation of intrinsic and scattering **Q** by envelope inversion). Our implementation uses the ObsPy library (Beyreuther *et al.* 2010) and several other libraries of the scientific Python ecosystem (NumPy, SciPy, statsmodels). It can easily be adapted to different local and regional setups by a

configuration file in JSON format. The script is published as open source at <http://www.github.com/trichter/qopen>.

4 APPLICATION TO MAGS2 DATA SET

The data collection and event localization was performed in the scope of the MAGS and MAGS2 projects. The event catalogue for Unterhaching was compiled by Megies & Wassermann (2014). Events for Landau and Insheim were located by Karlsruhe Institute of Technology (KIT) and Landesamt für Geologie und Bergbau of Rhineland-Palatinate. The events are located at a depth of around 3–5 km. Fig. 2 shows the station distribution and the epicentres of the analysed earthquakes for our study areas which are located in the Upper Rhine Graben and the Molasse basin.

For the calculation of modeled envelopes, we use the approximate solution of isotropic, acoustic radiative transfer of eq. (2). The mean S -wave velocity is determined from available local velocity models between the depth of the observed earthquakes and the surface. It is around 2400 m s^{-1} for the three sites. The mean density is set to 2700 kg m^{-3} . Earthquakes which occurred between 2013 October 1 and 2015 September 30 with a catalogue magnitude larger than 0.7 for Landau and Insheim and larger than 1.0 for Unterhaching are selected. The inversion is performed for each event separately to get statistics for the different target parameters. The corresponding data are prepared in the following way: instrument response is removed from the data. Data are filtered with a Butterworth filter in octave frequency bands (i.e. the higher corner frequency is twice the lower corner frequency) with central frequencies between 1.5 and 68 Hz. The bandpass filter has two corners and is applied once forward and once backward to guarantee zero phase shift. Envelopes are calculated with eqs (3) and (4). We use an assumed P -wave velocity of 4360 km s^{-1} and an S -wave velocity of 2400 km s^{-1} to calculate the P -onset and S -onset. We assured ourselves that the use of manual picks as onsets produces similar results. The average is calculated in each of the time windows (-40 s ; -30 s), (-30 s ; -20 s) and (-20 s ; -10 s) relative to

P -onset and the minimum of those three averages is used as the envelope noise level which is subtracted from the envelope data. The S -wave window starts 0.3 s before the S -onset and has a length of 1.5 s for Unterhaching and 4 s for Landau and Insheim. Visual inspection of the energy envelopes guarantees that the S -wave window covers the direct S wave and early coherent arrivals which are visible in a part of the envelopes. The coda window starts at the end of the corresponding S -wave window and ends 30 s (Landau, Insheim) or 10 s (Unterhaching) after the S -onset or until the envelope falls under a level of three times the signal-to-noise ratio. If the coda window is shorter than 2 s for Unterhaching or 4 s for Landau and Insheim, because the signal-to-noise ratio is quickly reached, data for this station are removed from the inversion. Defined time windows for Unterhaching are shorter because of the small extent of the station network in Unterhaching and the subsequent smaller station-hypocentre distances compared to the network in the Upper Rhine Graben. Data in the S -wave window are averaged. Furthermore, observed and modeled envelopes are smoothed with a 1 s wide Bartlett window. Finally, the inversion for intrinsic and scattering attenuation, site effects and spectral source energy is performed for all frequencies and events as described in Section 3 with a weight of the averaged S -wave data corresponding to the width of the S -wave window. Fig. 3 shows the resulting fits between observed and modeled energy envelopes for the inversion of the M1.4 event at Insheim on 2012 December 16 in the frequency band 8–16 Hz. We note that the maxima of smoothed observed and modeled envelopes do not overlap, because the chosen scattering Green's function does not correctly predict the shape of the envelope in the S -wave window. This demonstrates the necessity to average envelopes in the S -wave window. The final assessment of the scattering parameter $g^* = g_0$ (see Section 2) and the absorption parameter b is done by determining the robust geometric mean of the observations for each event. Robust statistics (Huber 2014) is used to account for outliers in our measurements. We use the median absolute deviation (MAD, normalization constant 0.67) as a scale parameter defining the spread of the distribution. The normalized MAD is not sensitive to outliers and corresponds to the standard deviation for normal

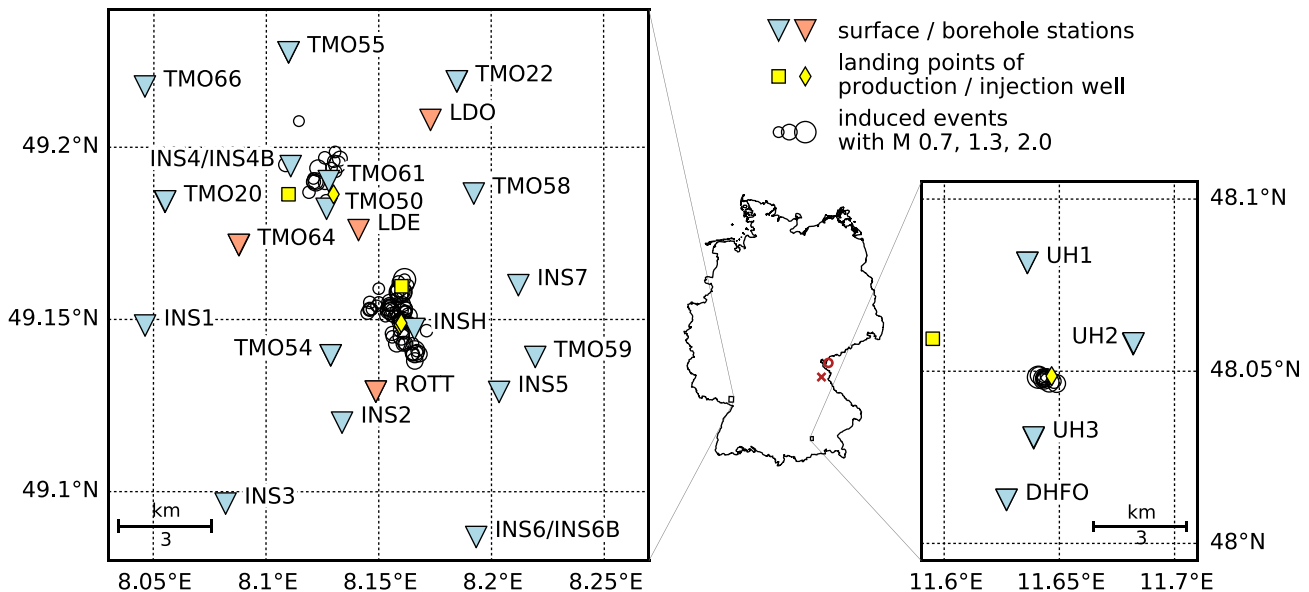


Figure 2. Map of Germany and maps of the two study areas located in the Upper Rhine Graben (left) and the Molasse basin (right). Displayed are the surface and borehole stations of the MAGS2 project, the earthquakes used in the inversion and the landing points of the wells of the three geothermal power plants of Landau (coordinates 49.187°N , 8.123°E , left plot), Insheim (coordinates 49.154°N , 8.154°E , left plot) and Unterhaching (right plot). The two crystalline sites to which results are compared are marked in the map of Germany (Continental Deep Drilling Programme—red cross, Vogtland area—red circle).

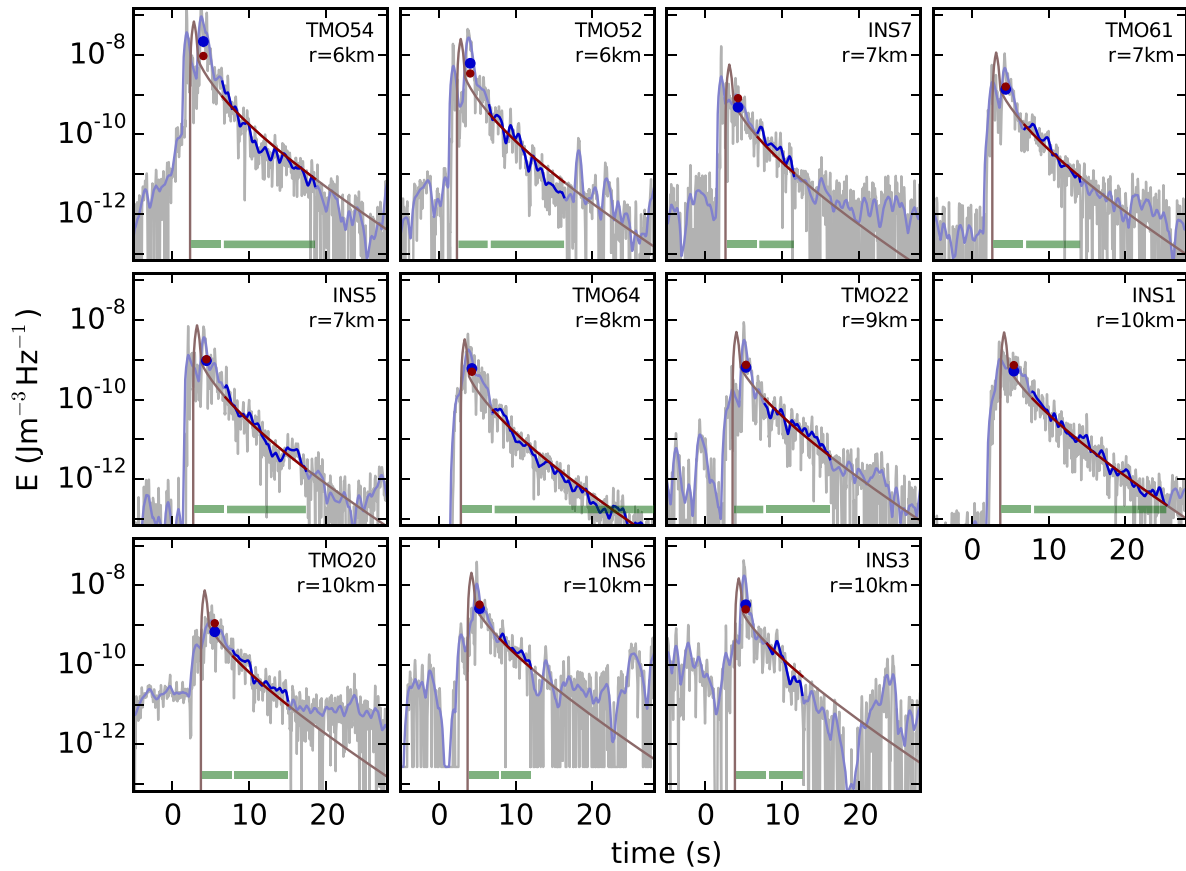


Figure 3. Fits between observed and modeled energy densities for the inversion of the M1.4 event at Insheim on 2012 December 16 in the frequency band 8–16 Hz. Displayed in each panel are the observed envelope (grey), the smoothed observed envelope (blue) and the smoothed modeled envelope (red). *S* wave and coda window are indicated with green bars. The mean of the observed and modeled envelope in the *S*-wave window is indicated with blue and red dots, respectively. Station name and distance to hypocentre is indicated in each panel.

distributed data. The robust mean is determined by the iteratively reweighted least-squares method. A first estimate of the iteratively determined robust mean is given by the ordinary mean. Data are weighted by Huber's t function with the tuning constant $t = 1.345$ and scaled by the MAD. The weights are 1 for $|x - x_{\text{mean}}| < t\text{MAD}$ and $t\text{MAD}/|x - x_{\text{mean}}|$ otherwise which effectively downweights outliers. The mean is calculated from the weighted data and can be used as the starting point for the next iteration. The procedure is repeated until convergence of the mean is reached.

Fig. 4 displays the results for the transport scattering coefficient g^* and absorption parameter b at the three analysed sites. At Unterhaching, the scattering parameter is around $1.6 \times 10^{-5} \text{ m}^{-1}$ (corresponding to a transport mean-free path of 60 km). For Landau and Insheim, the scattering parameter depends on frequency. It ranges from $4.2 \times 10^{-4} \text{ m}^{-1}$ (2 km) at 2 Hz for Landau and $1.6 \times 10^{-4} \text{ m}^{-1}$ (6 km) at 2 Hz for Insheim to $1.0 \times 10^{-5} \text{ m}^{-1}$ (90 km) at 30 Hz for both Landau and Insheim. For Landau, the observations at both extremes of the analysed frequencies are not trustworthy because of the low number of observations and large scatter of data. Still, results for Landau and Insheim are similar as these two study areas are located next to each other. The absorption constant depends on frequency, too. It describes a bell shape with a maximum at around 10 Hz for all three sites.

Station site corrections and spectral source energies are scaled by the solution of eq. (10) for each frequency and region to cor-

rect for the fact that partially a different set of stations is used in the inversions. Station site corrections are reproduced in Fig. A1 in Appendix. Site corrections for Landau scatter a lot because of the low number of observations. Site corrections for borehole stations (LDE, ROTT and TMO64) are on a relatively low level. The frequency dependence of the site corrections is related to the local subsurface structure at the stations. Source displacement spectra are calculated from the spectral source energies with eq. (11). It has to be noted, that source displacement spectra depend on the assumed frequency-independent value for the geometric mean of the site amplification factors. If the real mean site amplification factor is higher than 1, which is reasonable for sediments, the source displacement spectra must be downscaled accordingly. A real mean site amplification factor that depends on frequency adds another source of uncertainty. Source displacement spectra as a function of frequency are fitted by the source model in eq. (12) to obtain seismic moment M_0 , corner frequency f_c , high-frequency fall-off n and shape parameter γ for each event. We treat these source parameters as preliminary and use them to fix γ for each source region. The shape parameter γ is 1.1 ± 0.9 for Landau, 1.5 ± 1.3 for Insheim and 0.53 ± 0.24 for Unterhaching (reported are robust mean and median standard deviation). The fitting of the source model to the observed spectra is repeated for fixed γ to finally assess the parameters M_0 , f_c and n for each event. γ is assumed to be 1.3 for Landau and Insheim. The average high-frequency fall-off is $n = 3.2 \pm 0.8$

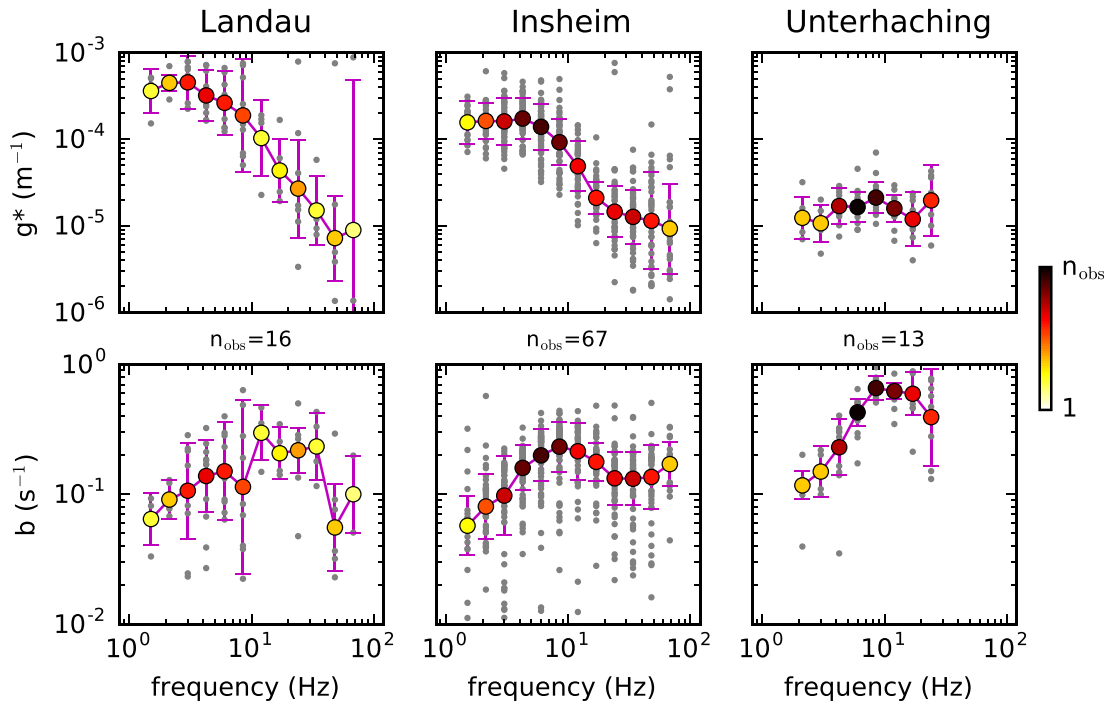


Figure 4. Results of the inversion procedure for the three investigated data sets consist of the transport scattering coefficient (top) and intrinsic attenuation coefficient (bottom) as a function of frequency for Landau, Insheim and Unterhaching. Grey dots indicate the results for individual measurements of a single event. The circles with error bars correspond to the robust mean and median absolute deviation (MAD) of the observations for each frequency band. The number of samples in each frequency band is colour-coded relative to the number of used events for this site ($n_{\text{obs}} = 16, 67$ and 13 for Landau, Insheim and Unterhaching, respectively).

for Landau, $n = 3.0 \pm 0.3$ for Insheim and $n = 4.7 \pm 0.5$ for Unterhaching. Our data sets only span a narrow range of seismic moments. It is therefore adequate to report average corner frequencies despite their scaling with seismic moment. The average corner frequency is $f_c = (8.4 \pm 3.0)\text{Hz}$ for Landau, $f_c = (9.2 \pm 1.8)\text{Hz}$ for Insheim and $f_c = (12.4 \pm 1.3)\text{Hz}$ for Unterhaching. n and f_c for Unterhaching are not well constrained, because result parameters were only obtained for frequencies up to 24Hz . Observed source displacement spectra and fitted source models for each event are reproduced in Fig. A2 in Appendix. Determined seismic moment, corner frequency and high-frequency fall-off are indicated in the plots. Fig. 5 shows all measured source displacement spectra with fitted source models for the Upper Rhine Graben (Landau and Insheim). A representative source model with $f_c = 9.1\text{Hz}$ and $n = 3.0$ is indicated with a black line.

5 DISCUSSION

In Fig. 6, we compare the inverse of the quality factors for intrinsic and scattering attenuation at different sites in Germany and the Czech Republic. Q values for our results were calculated with eq. (15). We compare results from three locations dominated by sediments (Landau, Insheim, Unterhaching) and two locations dominated by crystalline rock [Czech-German border region Vogtland, Continental Deep Drilling Programme (KTB)]. Results for the Vogtland area were obtained using the method of this paper (compare Gaebler *et al.* 2015). Results for the KTB were taken from table 2 of Fielitz & Wegler (2015). Fig. 6 additionally shows the total attenuation $Q_{\text{tot}}^{-1} = Q_{\text{sc}}^{-1} + Q_{\text{i}}^{-1}$ and the seismic albedo $B_0 = Q_{\text{sc}}^{-1}/Q_{\text{tot}}^{-1}$ expressing the contribution of scattering to the total attenuation.

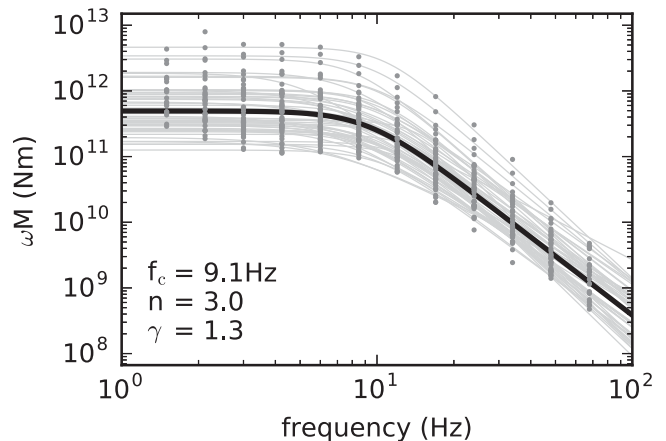


Figure 5. Observed source displacement spectra (grey dots) and fitted source models (grey lines) for the Upper Rhine Graben. The black line represents a representative source model whose parameters f_c and n are averaged over all individual source models.

The quality factor for intrinsic attenuation is constant for S -wave propagation in sediments at frequencies smaller than 8Hz . It is around 100 for Unterhaching and 160 for Landau and Insheim with lower attenuation above 10Hz . The plateau and decrease of S -wave intrinsic attenuation might allow for conclusions on the value of relaxation times which itself depend on the physical dimensions of the elements in the rock (Sato *et al.* 2012, p. 156). In contrast, Q_{i}^{-1} is strictly monotonic decreasing for S waves in crystalline rock. Furthermore, intrinsic attenuation is on a higher level for the sedimentary sites than for the crystalline sites for the compared data sets and frequencies above 2Hz .

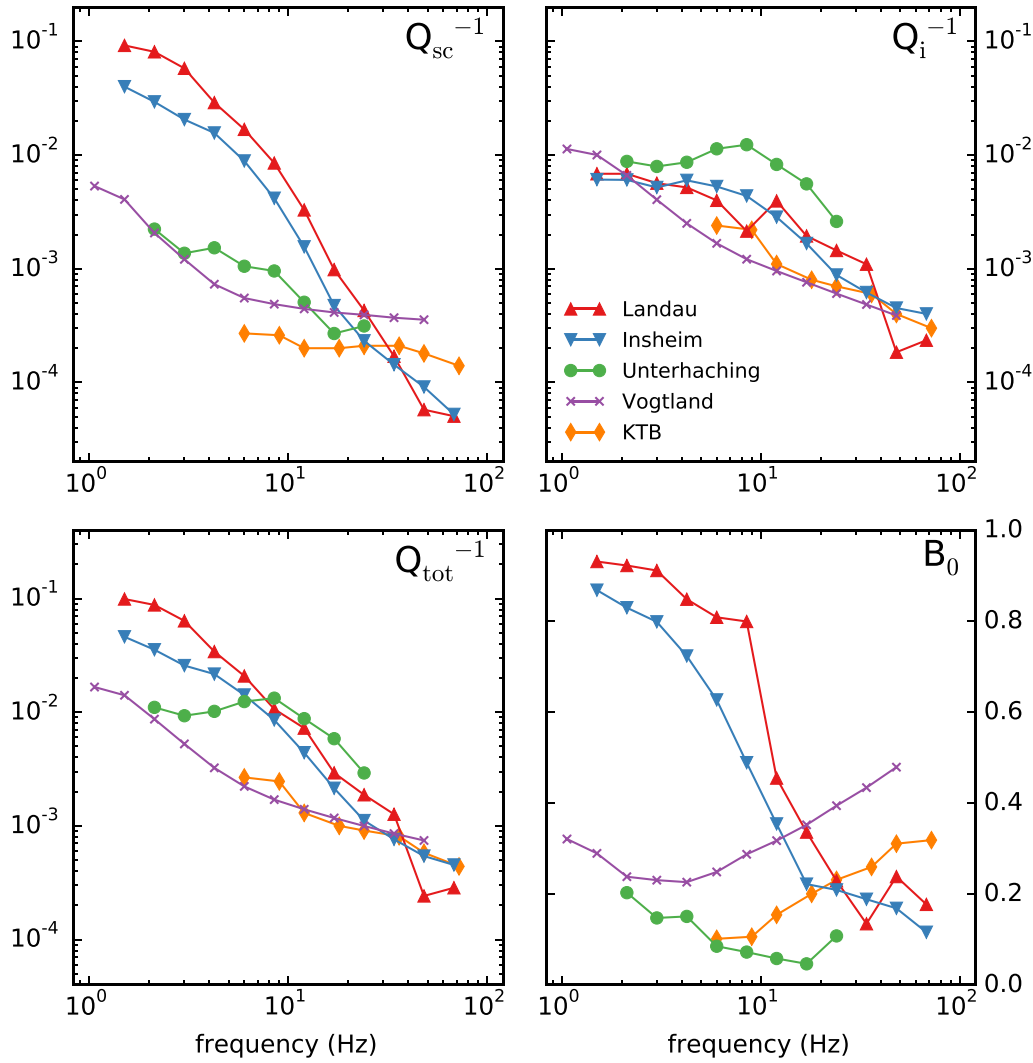


Figure 6. Comparison of the inverse quality factors Q^{-1} for scattering attenuation (top left), intrinsic attenuation (top right), total attenuation (lower left) and seismic albedo B_0 (lower right) at different sites in Germany and Czech Republic. The values for Landau, Insheim and Unterhaching are calculated with eq. (15) from the coefficients in Fig. 4. Q values for the Vogtland are calculated with the same method as described in this paper. Q values for the Continental Deep Drilling Programme (KTB) are taken from table 2 of Fielitz & Wegler (2015).

The inverse of the quality factor for scattering is generally lower than the corresponding values for intrinsic attenuation. Intrinsic attenuation therefore dominates over scattering. There is one exception to this observation: the two sites located in the Upper Rhine Graben show an exceptional high scattering coefficient for low frequencies. Scattering is therefore the dominant attenuation process for low frequencies in the Upper Rhine Graben. The balance point, where both mechanisms contribute equally to the attenuation, is at around 10 Hz. A further observation is the exceptional high decrease of $Q_{sc}^{-1} \propto f^{-1.9}$ for the Upper Rhine Graben. In contrast, the decrease of the inverse of the scattering quality factor is around $Q_{sc}^{-1} \propto f^{-0.9}$ for Unterhaching, $Q_{sc}^{-1} \propto f^{-0.7}$ for the Vogtland region and around $Q_{sc}^{-1} \propto f^{-0.2}$ for KTB. Total attenuation is best described by the power laws reported in Table 1. The frequency dependence of total attenuation for Unterhaching is not well represented by a fitted power law. Total attenuation for the sites located in crystalline rocks is lower than for those located in sedimentary rocks.

Table 1. Best-fitting power laws for total attenuation Q_{tot}^{-1} as a function of frequency.

| Location | Power law for Q_{tot}^{-1} |
|--------------|------------------------------|
| Landau | $0.33 \times f^{-1.67}$ |
| Insheim | $0.11 \times f^{-1.35}$ |
| Unterhaching | $0.019 \times f^{-0.41}$ |
| Vogtland | $0.014 \times f^{-0.86}$ |
| KTB | $0.0096 \times f^{-0.73}$ |

For Insheim, there seems to be a transition between a higher value of the scattering coefficient at low frequencies and a lower value for high frequencies (Fig. 4). Because of larger errors, this observation is unincisive for Landau. The addressed transition manifests in a change in the slope for data points corresponding to Insheim in Fig. 6 and might indicate a variation of the scattering coefficient with depth, for example, due to the interface between sediments and bedrock.

The limitations of the applied source and scattering model as well as the assumption of a homogeneous half-space have to be discussed. The used peak-like source function is an adequate assumption for the small earthquakes used in this study. The radiation pattern which is neglected by the source model does have only a minor influence on the S -wave coda due to multiple scattering. Its influence on the direct S wave may distort attenuation estimates if the station distribution covers only a part of the azimuthal range relative to the earthquakes. The networks used in this study show a good azimuthal coverage. It is therefore not expected that the source radiation pattern has an influence on the attenuation estimates. The propagation and scattering is described by the acoustic isotropic radiative transfer theory and the corresponding scattering Green's function. The restriction to S waves and the consequent usage of the acoustic approximation is justified by the high ratio of S -to- P versus P -to- S scattering conversion. The assumption of isotropic scattering is not correct but is a simple and effective way of describing the transport for the anisotropic case by interpreting the obtained scattering coefficient as transport scattering coefficient (Gaebler *et al.* 2015). The inaccuracy of the used Green's function in the S -wave window is dealt with by averaging in this time window. This also removes any information in the observed envelopes from which the scattering coefficient g_0 could be determined. Anyway, this is not the scope of this study as different investigations have shown that it is difficult to estimate the scattering coefficient beyond its restriction to wide ranges in the forward scattering regime (Hoshiba 1995; Gusev & Abubakirov 1996; Calvet & Margerin 2013; Gaebler *et al.* 2015). Finally, the assumption of a homogeneous half-space is not adequate and therefore the estimates reported here are a representation of the average attenuation properties over a crustal layer. We exclude any influence of the Moho contrast to our estimates as reported by Margerin *et al.* (1999). Assuming a Moho depth of 30 km and a mean S -wave velocity in the crust of 3 km s^{-1} energy leakage through the Moho may be observed only for traveltimes larger than 20 s. However, most of the envelopes are fitted in a time window which is cut before 20 s traveltimes, because the signal-to-noise ratio is reached earlier.

The presented method allows to determine the source displacement spectra of local and regional events. Source parameters (seismic moment, corner frequency, high-frequency fall-off) can be obtained by fitting the underlying source model. The usual approach determines source parameters from displacement spectra observed at stations. In this case, attenuation affects the displacement spectra by a factor $\exp(-\pi f t Q^{-1})$ with traveltimes t and total attenuation $Q = Q_{\text{tot}}$. Commonly, the omega-square model ($n = 2$) observed for large earthquakes is equally applied to small earthquakes and Q is assumed to be a simple function of frequency (constant or power law). Then, the displacement spectra observed at stations can be inverted for seismic moment, corner frequency and Q (e.g. Masuda & Suzuki 1982; Hough *et al.* 1999; Michálek & Fischer 2013). However one or both assumptions may be inadequate. Determining attenuation independently, we observe a high-frequency fall-off greater than or equal to 3 for all three studied sites. The deviation from the omega square model may be due to the reservoir-induced nature of the earthquakes. Similar observation have been reported by Ambeh & Fairhead (1991) obtaining a high-frequency fall-off between 3 and 5 for most events. These results may suggest that the omega-square model as a source model for small earthquakes has to be revisited in its universal adoption. If station displacement spectra with high-frequency fall-off $n > 2$ were inverted for Q under the assumption of $n = 2$, a good fit would be produced anyway because of the high trade-off between Q and n . However, this may

distort the estimates of corner frequency and even seismic moment especially if the assumed frequency dependence of Q is not correct. We therefore advocate to use independently obtained estimates of Q when inverting station displacement spectra for source parameters or to remove path effects including attenuation with the help of empirically determined Green's functions (Mueller 1985).

6 CONCLUSIONS

We presented an improved method to separate intrinsic and scattering attenuation of seismic shear waves by envelope inversion. The advantages over the original approach are the simultaneous determination of site corrections and spectral source densities together with the intrinsic attenuation constant, the equal treatment of both used time windows and a generalization to more than one event. A script is provided which enables scientists to easily determine scattering and intrinsic attenuation parameters with the help of local or regional seismicity. Additionally, the energy site amplification at used stations and the source displacement spectra of used events can be estimated by the script.

We determined intrinsic and scattering attenuation coefficients of shear waves near three geothermal reservoirs in Germany for frequencies between 1 and 70 Hz. Intrinsic and scattering Q -values of these three sites located in sediments and two sites located in crystalline rock are compared. Intrinsic attenuation is the dominant attenuation mechanism except for dominant scattering in the Upper Rhine Graben at frequencies below 10 Hz. The transition between the plateau and decrease of the inverse quality factor for intrinsic attenuation for the sedimentary sites could be a subject of further research. Another open question is the nature of the high and partially changing slope of the frequency dependence of the quality factor for scattering in the Upper Rhine Graben.

The source displacement spectra we obtained show a high-frequency fall-off greater than or equal to 3 and indicate the invalidity of the omega square model for our data set. We think further studies are necessary exploring the range of high-frequency fall-off parameters of source displacement spectra with the help of independently determined attenuation parameters. Linking the high-frequency fall-off to different species of earthquakes might lead to a better understanding of possible source mechanisms.

ACKNOWLEDGEMENTS

We acknowledge support of the Bundesministerium für Wirtschaft und Energie (BMWi) under the grant MAGS2: 0325662A. We thank two anonymous reviewers whose comments helped to improve the manuscript considerably.

REFERENCES

- Abercrombie, R.E., 1995. Earthquake source scaling relationships from -1 to 5 M_L using seismograms recorded at 2.5-km depth, *J. geophys. Res.*, **100**(B12), 24 015–24 036.
- Ambeh, W. & Fairhead, J., 1991. Spectral characteristics and source parameters of microearthquakes from the Mt Cameroon volcanic region, West Africa, *Geophys. J. Int.*, **106**(1), 229–237.
- Beyreuther, M., Barsch, R., Krischer, L., Megies, T., Behr, Y. & Wassermann, J., 2010. ObsPy: a Python toolbox for Seismology, *Seismol. Res. Lett.*, **81**(3), 530–533.
- Calvet, M. & Margerin, L., 2013. Lapse-time dependence of coda Q : anisotropic multiple-scattering models and application to the Pyrenees, *Bull. seism. Soc. Am.*, **103**(3), 1993–2010.

- Emoto, K., Sato, H. & Nishimura, T., 2010. Synthesis of vector wave envelopes on the free surface of a random medium for the vertical incidence of a plane wavelet based on the Markov approximation, *J. geophys. Res.*, **115**, 1–15.
- Fehler, M., Hoshihara, M., Sato, H. & Obara, K., 1992. Separation of scattering and intrinsic attenuation for the Kanto-Tokai region, Japan, using measurements of S-wave energy versus hypocentral distance, *Geophys. J. Int.*, **108**(3), 787–800.
- Fielitz, D. & Wegler, U., 2015. Intrinsic and scattering attenuation as derived from fluid induced microseismicity at the German Continental Deep Drilling site, *Geophys. J. Int.*, **201**(3), 1346–1361.
- Gäbler, P.J., Eulenfeld, T. & Wegler, U., 2015. Seismic scattering and absorption parameters in the W-Bohemia/Vogtland region from elastic and acoustic radiative transfer theory, *Geophys. J. Int.*, **203**(3), 1471–1481.
- Gusev, A.A. & Abubakirov, I.R., 1996. Simulated envelopes of non-isotropically scattered body waves as compared to observed ones: another manifestation of fractal heterogeneity, *Geophys. J. Int.*, **127**(1), 49–60.
- Hanks, T.C. & Kanamori, H., 1979. A moment magnitude scale, *J. geophys. Res.*, **84**, 2348–2350.
- Hoshihara, M., 1995. Estimation of nonisotropic scattering in western Japan using coda wave envelopes: application of a multiple nonisotropic scattering model, *J. geophys. Res.*, **100**(B1), 645–657.
- Hoshihara, M., Sato, H. & Fehler, M., 1991. Numerical basis of the separation of scattering and intrinsic absorption from full seismogram envelope: a Monte-Carlo simulation of multiple isotropic scattering, *Pap. Meteorol. Geophys.*, **42**(2), 65–91.
- Hough, S.E., Lees, J.M. & Monastero, F., 1999. Attenuation and source properties at the Coso geothermal area, California, *Bull. seism. Soc. Am.*, **89**(6), 1606–1619.
- Huber, P.J., 2014. Robust Statistics, in *International Encyclopedia of Statistical Science*, pp. 1248–1251, ed. Lovric, M., Springer.
- Margerin, L., Campillo, M., Shapiro, N.M. & Van Tiggelen, B., 1999. Residence time of diffuse waves in the crust as a physical interpretation of coda Q: application to seismograms recorded in Mexico, *Geophys. J. Int.*, **138**(2), 343–352.
- Masuda, T. & Suzuki, Z., 1982. Objective estimation of source parameters and local Q values by simultaneous inversion method, *Phys. Earth planet. Inter.*, **30**(2–3), 197–208.
- Megies, T. & Wassermann, J., 2014. Microseismicity observed at a non-pressure-stimulated geothermal power plant, *Geothermics*, **52**, 36–49.
- Michálek, J. & Fischer, T., 2013. Source parameters of the swarm earthquakes in West Bohemia/Vogtland, *Geophys. J. Int.*, **195**(2), 1196–1210.
- Mueller, C.S., 1985. Source pulse enhancement by deconvolution of an empirical Green's function, *Geophys. Res. Lett.*, **12**(1), 33–36.
- Paasschens, J., 1997. Solution of the time-dependent Boltzmann equation, *Phys. Rev. E*, **56**(1), 1135–1141.
- Padhy, S., Wegler, U. & Korn, M., 2007. Seismogram envelope inversion using a multiple isotropic scattering model: application to aftershocks of the 2001 Bhuj earthquake, *Bull. seism. Soc. Am.*, **97**(1B), 222–233.
- Sato, H., Fehler, M.C. & Maeda, T., 2012. *Seismic Wave Propagation and Scattering in the Heterogeneous Earth*, 2nd edn, Springer.
- Sens-Schönfelder, C. & Wegler, U., 2006. Radiative transfer theory for estimation of the seismic moment, *Geophys. J. Int.*, **167**(3), 1363–1372.
- Ugalde, A. & Carcolé, E., 2009. Comments on “Separation of Q_i and Q_s from passive data at Mt. Vesuvius: a reappraisal of the seismic attenuation estimates” by E. Del Pezzo *et al.* (2006), *Phys. Earth planet. Inter.*, **173**(1–2), 191–194.
- Wegler, U., Korn, M. & Przybilla, J., 2006. Modeling full seismogram envelopes using radiative transfer theory with born scattering coefficients, *Pure appl. Geophys.*, **163**(2–3), 503–531.
- Zeng, Y., Su, F. & Aki, K., 1991. Scattering wave energy propagation in a random isotropic scattering medium: 1. Theory, *J. geophys. Res.*, **96**(B1), 607–619.

APPENDIX A: STATION SITE CORRECTIONS AND SOURCE DISPLACEMENT SPECTRA OF THE MAGS2 DATA SET

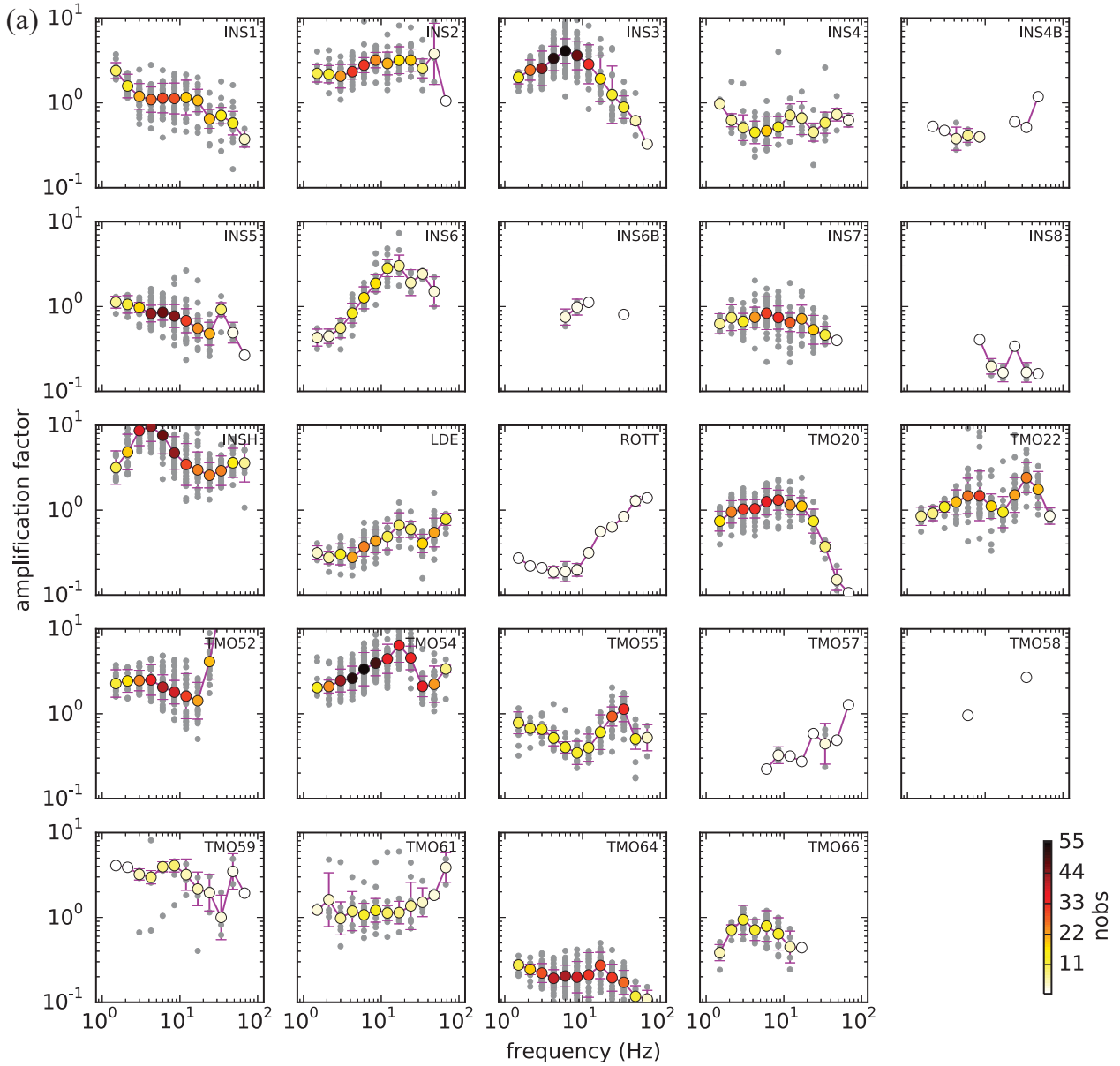


Figure A1. Reported energy site amplification factors for Insheim (a), Landau (b) and Unterhaching (c). Observations for individual events are represented by grey dots. Median absolute deviation as a measure of the spread of the observations and the robust mean (compare also Section 4 of the paper) are indicated by error bars and circles. The filling colour of the circle represents the number of used events for this frequency band.

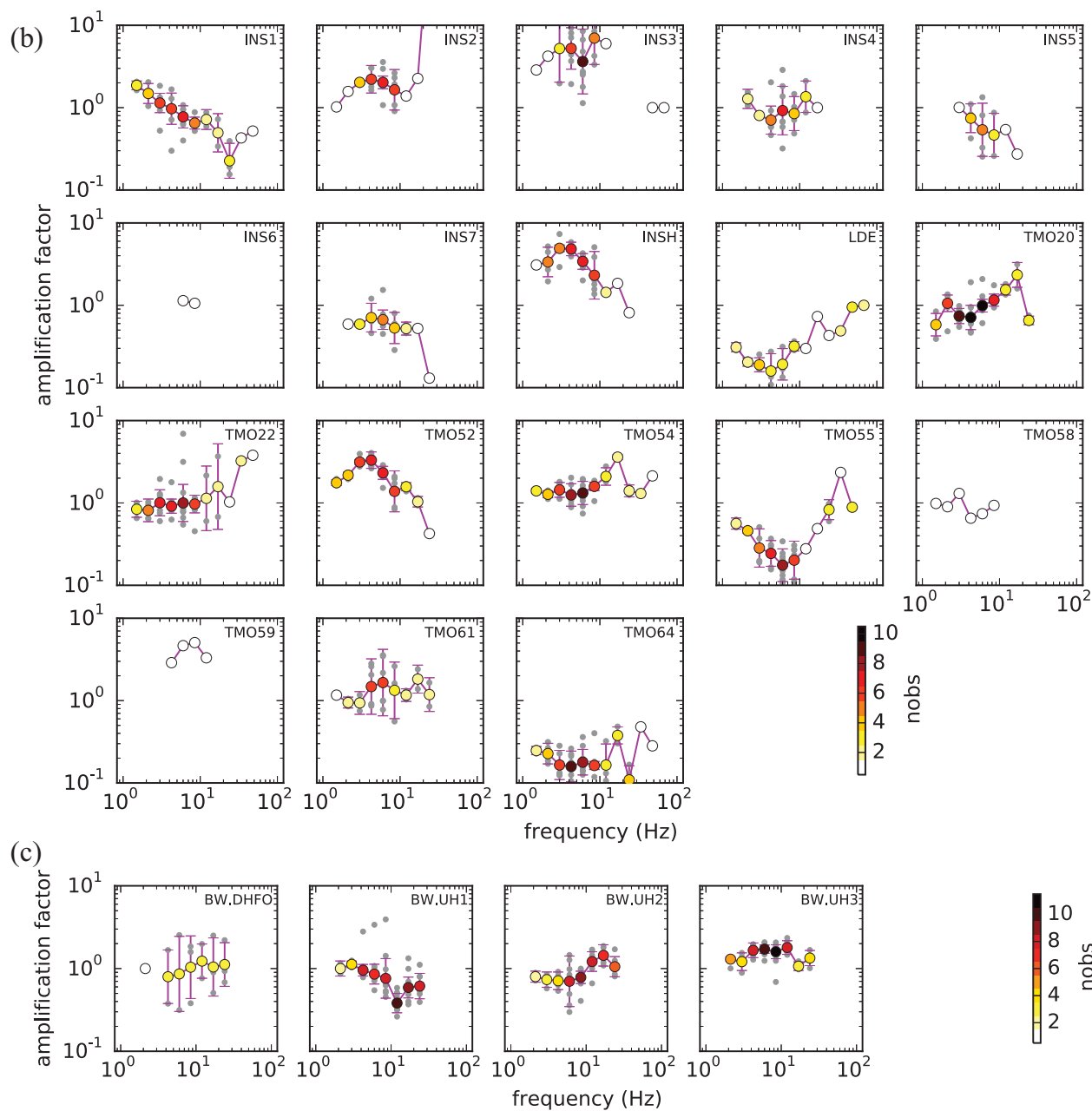


Figure A1 (Continued.)

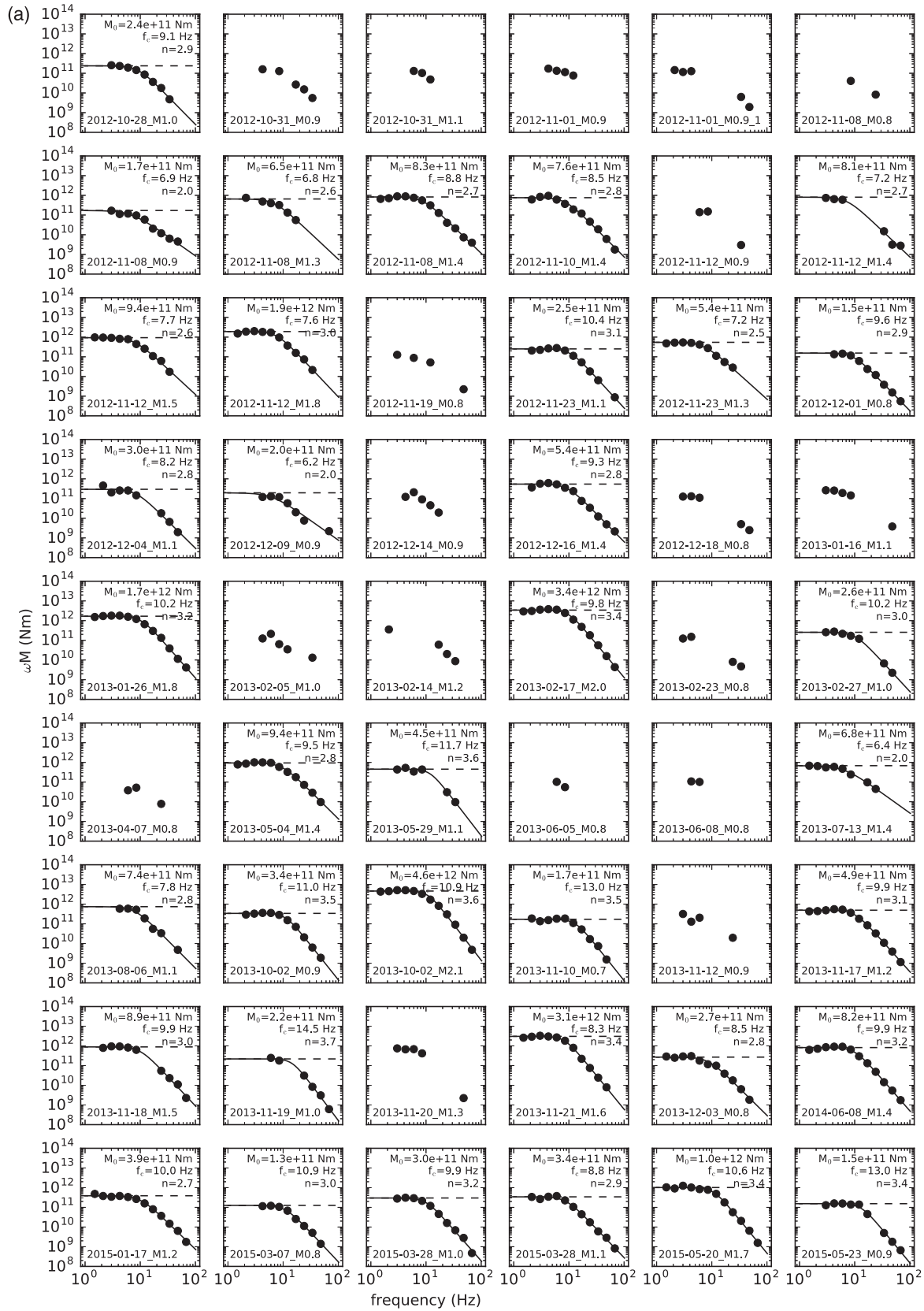


Figure A2. Source displacement spectra for Insheim (a), Landau (b) and Unterhaching (c). Solid lines represent fitted source models (eq. 12). The low-frequency trends of the source models, that is, the seismic moments, are indicated by dashed lines. Seismic moment M_0 , corner frequency f_c and high-frequency fall-off n are printed for each source model into the corresponding panel. The shape parameter is $\gamma = 1.3$ for Insheim and Landau and $\gamma = 0.53$ for Unterhaching. The indicated events consist of date and catalogue magnitude.

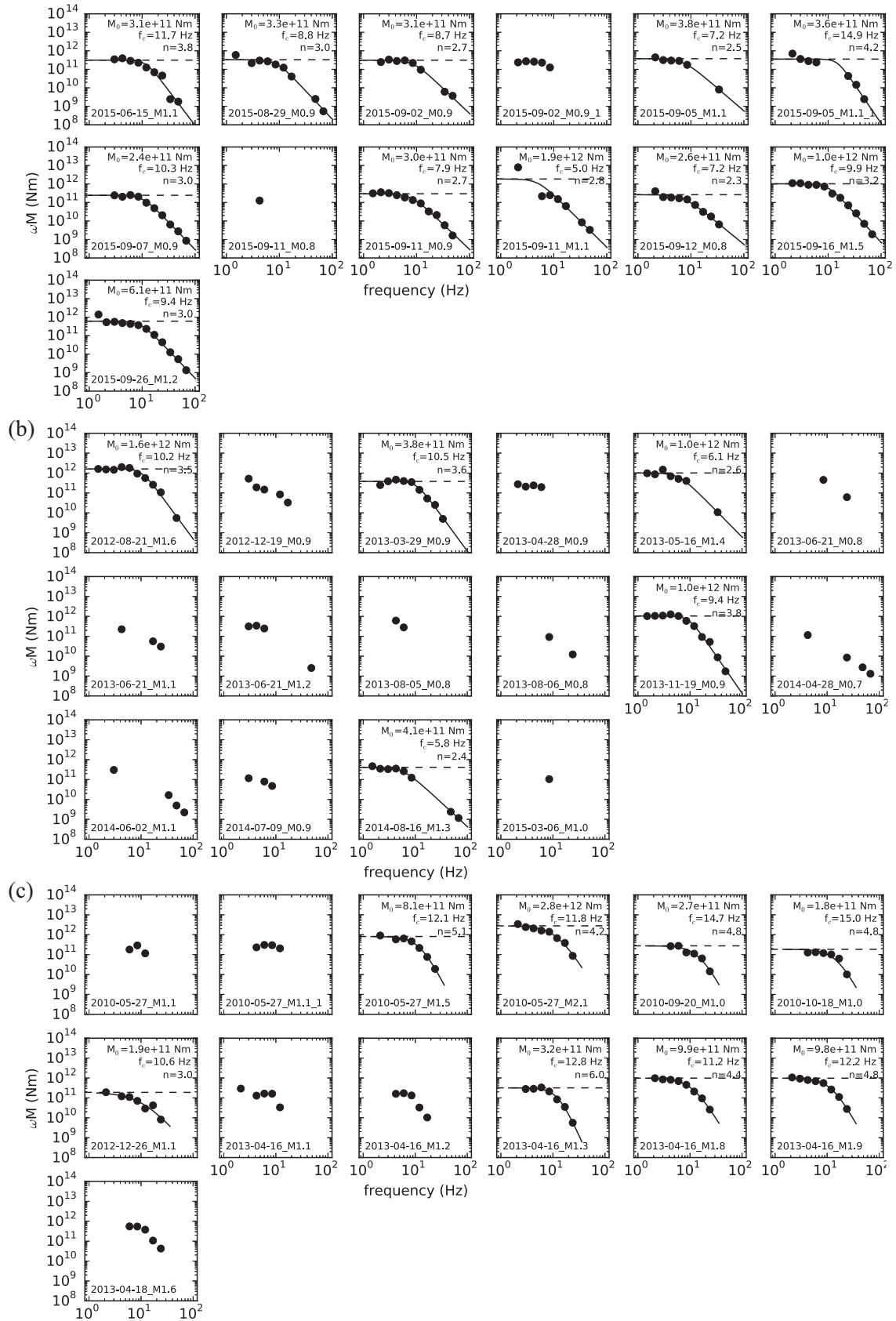


Figure A2 (Continued.)